




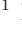

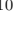




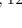













The James Webb Interferometer: Space-based interferometric detections of PDS 70 b and c at 4.8 μm

DORI BLAKELY ^{1,2} DOUG JOHNSTONE ^{2,1} GABRIELE CUGNO ³ ANAND SIVARAMAKRISHNAN ^{4,5,6}
PETER TUTHILL ⁷ RUOBING DONG ¹ BENJAMIN J. S. POPE ^{8,9} LOÏC ALBERT ¹⁰ MAX CHARLES ⁷
RACHEL A. COOPER ⁴ MATTHEW DE FURIO ¹¹ LOUIS DESDOIGTS ⁷ RENÉ DOYON ^{10,12} LOGAN FRANCIS ¹³
ALEXANDRA Z. GREENBAUM ¹⁴ DAVID LAFRENIÈRE ¹⁰ JAMES P. LLOYD ¹⁵ MICHAEL R. MEYER ³
LAURENT PUEYO ⁴ SHRISHMOY RAY ⁸ JOEL SÁNCHEZ-BERMÚDEZ ^{16,17} ANTHONY SOULAIN ¹⁸
DEEPASHRI THATTE ⁴ AND THOMAS VANDAL ¹⁰

¹Department of Physics and Astronomy, University of Victoria, 3800 Finnerty Road, Elliot Building, Victoria, BC, V8P 5C2, Canada

²NRC Herzberg Astronomy and Astrophysics, 5071 West Saanich Road, Victoria, BC, V9E 2E7, Canada

³Department of Astronomy, University of Michigan, Ann Arbor, MI 48109, USA

⁴Space Telescope Science Institute, 3700 San Martin Drive, Baltimore, MD 21218, USA

⁵Astrophysics Department, American Museum of Natural History, 79th Street at Central Park West, New York, NY 10024

⁶Department of Physics and Astronomy, Johns Hopkins University, 3701 San Martin Drive, Baltimore, MD 21218, USA

⁷Sydney Institute for Astronomy, School of Physics, University of Sydney, NSW 2006, Australia

⁸School of Mathematics and Physics, University of Queensland, St Lucia, QLD 4072, Australia

⁹University of Southern Queensland, Centre for Astrophysics, Toowoomba, Queensland, Australia

¹⁰Trottier Institute for Research on Exoplanets, Département de Physique, Université de Montréal, 1375 Ave Thérèse-Lavoie-Roux, Montréal, QC, H2V 0B3, Canada

¹¹Department of Astronomy, The University of Texas at Austin, 2515 Speedway Stop C1400, Austin, TX 78712, USA

¹²Observatoire du Mont-Mégantic, Université de Montréal, Montréal H3C 3J7, Canada

¹³Leiden Observatory, Leiden University, PO Box 9513, 2300 RA Leiden, The Netherlands

¹⁴IPAC, Caltech, 1200 E. California Blvd., Pasadena, CA 91125, USA

¹⁵Carl Sagan Institute/Department of Astronomy, Cornell University, Ithaca NY 14853

¹⁶Instituto de Astronomía, Universidad Nacional Autónoma de México, Apdo. Postal 70264, Ciudad de México, 04510, México

¹⁷Max-Planck-Institut für Astronomie, Königstuhl 17, D-69117 Heidelberg, Germany

¹⁸Univ. Grenoble Alpes, CNRS, IPAG, 38000 Grenoble, France

ABSTRACT

We observed the planet-hosting system PDS 70 with the James Webb Interferometer, JWST’s Aper-
ture Masking Interferometric (AMI) mode within NIRISS. Observing with the F480M filter centered
at 4.8 μm , we simultaneously fit a geometric model to the outer disk and the two known planetary
companions. We re-detect the protoplanets PDS 70 b and c at an SNR of 21 and 11, respectively.
Our photometry of both PDS 70 b and c provide evidence for circumplanetary disk emission through
fitting SED models to these new measurements and those found in the literature. We also newly detect
emission within the disk gap at an SNR of ~ 4 , at a position angle of 207^{+11}_{-10} degrees, and an uncon-
strained separation within ~ 200 mas. Follow-up observations will be needed to determine the nature
of this emission. We place a 5σ upper limit of $\Delta\text{mag} = 7.56$ on the contrast of the candidate PDS 70
d at 4.8 μm , which indicates that if the previously observed emission at shorter wavelengths is due to
a planet, this putative planet has a different atmospheric composition than PDS 70 b or c. Finally, we
place upper limits on emission from any additional planets in the disk gap. We find an azimuthally
averaged 5σ upper limit of $\Delta\text{mag} \approx 7.5$ at separations greater than 125 mas. These are the deepest
limits to date within ~ 250 mas at 4.8 μm and the first space-based interferometric observations of this
system.

1. INTRODUCTION

PDS 70 is one of the most extensively studied young
stellar systems. It is the only known multi-planet pro-
toplanetary disk system, where two or more planets
have been robustly detected within the disks from which

they formed (Keppler et al. 2018; Haffert et al. 2019).
The disk consists of a large outer component and a
smaller inner component (Keppler et al. 2018), sepa-
rated by a wide cavity (Hashimoto et al. 2012; Facchini
et al. 2021) spanning between $\lesssim 17$ au and ~ 54 au (Kep-

pler et al. 2018). The inner disk was first inferred via spectral energy distribution (SED) fitting (Hashimoto et al. 2012; Dong et al. 2012), and was subsequently isolated in the near-infrared (Keppler et al. 2018) and sub-millimeter (Keppler et al. 2019). Recently observations with JWST/MIRI detected water vapour in the inner disk (Perotti et al. 2023). The outer disk of PDS 70 is not significantly perturbed in contrast to some other protoplanetary disk systems where planet candidates have been detected, such as MWC 758 (Wagner et al. 2023) or AB Aurigae (Currie et al. 2022). The PDS 70 outer disk appears as a close to symmetric ring at sub-mm wavelengths (Keppler et al. 2019; Benisty et al. 2021), with one significant azimuthal asymmetry observed to the north-west of the star that is close to coincident with an arm-like structure seen in the near-infrared (Wang et al. 2020; Juillard et al. 2022).

The planets PDS 70 b and c have been extensively imaged in the near-infrared from ~ 1 to $3.8 \mu\text{m}$ (e.g., Keppler et al. 2018; Müller et al. 2018; Mesa et al. 2019; Christiaens et al. 2019; Wang et al. 2020, 2021b; Cugno et al. 2021), with a few detections beyond $\sim 4 \mu\text{m}$ to $4.8 \mu\text{m}$ (Stolker et al. 2020a; Christiaens et al. 2024), as well as detections in H_α (Wagner et al. 2018; Haffert et al. 2019). Circumplanetary disk emission from PDS 70 c has been directly detected in the sub-mm with ALMA, coincident with detections in the near-infrared (Isella et al. 2019; Benisty et al. 2021). Sub-mm emission has also been observed that is seemingly associated with PDS 70 b, however it is offset from the near-infrared detections (Isella et al. 2019; Benisty et al. 2021). Additionally, emission at the L_5 Lagrangian point of PDS 70 b has tentatively been detected in the sub-mm with ALMA (Balsobre-Ruza et al. 2023). Finally, a third point source has been tentatively detected in the PDS 70 disk cavity, using VLT/SPHERE over multiple epochs (Mesa et al. 2019). The nature of the source is still not well understood as it has a distinct spectrum compared to both PDS 70 b and c, more similar to the spectrum of PDS 70 A between ~ 1 - $1.6 \mu\text{m}$, implying it may be scattered light (Mesa et al. 2019). This source was tentatively re-detected at $1.9 \mu\text{m}$ with JWST/NIRCam (Christiaens et al. 2024).

Many atmospheric models of massive giant planets predict a drop in flux in the mid-infrared beyond $\sim 4.5 \mu\text{m}$ compared to between 2 - $2.5 \mu\text{m}$ and 3 - $4 \mu\text{m}$, so observations at $4.8 \mu\text{m}$ may allow for excess emission from warm circumplanetary disk (CPD) dust to be inferred. Wang et al. (2021b) showed that the VLT/NACO M' detection of PDS 70 b from Stolker et al. (2020a) provided weak support for excess blackbody-like emission, so follow up observations at $\sim 4.8 \mu\text{m}$ and beyond will

allow for this tentative detection of CPD emission in the mid-infrared to be confirmed. Recently, Christiaens et al. (2024) re-detected PDS 70 b and c with the JWST/NIRCam ($4.8 \mu\text{m}$) F480M filter. Their detection of PDS 70 b was in agreement with the M' detection, but with a larger uncertainty.

In our work, we re-detect PDS 70 b and c at F480M using the James Webb Interferometer, an independent method to Christiaens et al.’s JWST/NIRCam results, and make the most precise measurement of the flux of PDS 70 b at $4.8 \mu\text{m}$, using the JWST/NIRISS F480M filter. We also detect PDS 70 c using the F480M filter at a similar precision to Christiaens et al. (2024), after including our conservative systematic noise estimation in our error budget. Wang et al. (2021b) made the first interferometric detection of PDS 70 b and c from the ground, using VLTI/GRAVITY. Here, using the power of the James Webb Interferometer, we detect PDS 70, its outer disk, and its two protoplanets, b and c. These are the first planets detected with space-based interferometry.

This paper is structured as follows: §2 outlines the data acquisition, reduction and cleaning procedure; §3 details the disk plus two planet model fitting and the conversion of the measured contrasts to fluxes; §4 outlines the derived planet parameters and the analysis of the data for any signal beyond the two known planets and the disk; §5 discusses the implications of the measured contrasts and the nature of the tentative detection of residual emission in the data. We close with a summary in §6.

2. OBSERVATIONS AND DATA REDUCTION

We observed PDS 70 as a part of the NIRISS GTO program (PID 1242, PI D. Johnstone). The data presented in this paper were acquired on February 24 2023 using the James Webb Interferometer, the aperture masking interferometry mode of the NIRISS instrument (Sivaramakrishnan et al. 2012, 2023; Doyon et al. 2023) henceforth referred to as AMI, in the F480M filter ($\lambda = 4.815 \mu\text{m}$, $\Delta\lambda = 0.298 \mu\text{m}$)¹. The SUB80 sub-array was used along with the NISRAPID readout pattern. The point-spread-function (PSF) calibrator star HD 123991 was also observed using the same configuration. Both targets were observed using no dithers and no rolls. The PDS 70 data set consists of 96 groups and 418 integrations, while the brighter HD 123991 data set consists of 29 groups and 418 integrations. This corre-

¹ <https://jwst-docs.stsci.edu/jwst-near-infrared-imager-and-slitless-spectrograph/niriss-instrumentation/niriss-filters>

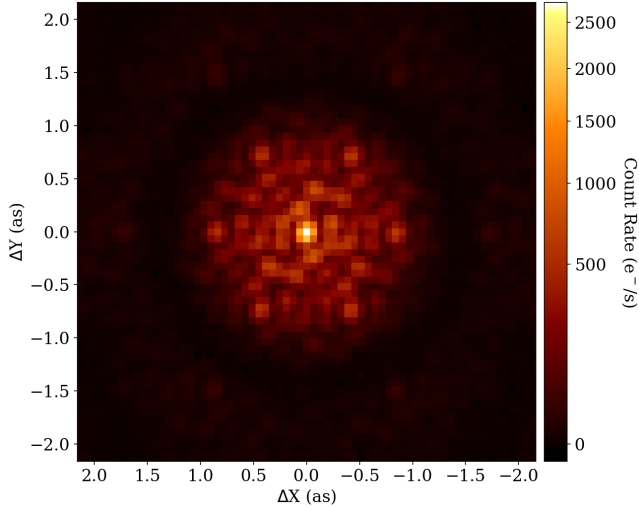


Figure 1. Mean PDS 70 `calints` file, after bad pixel correction, using only the first 28 groups.

sponds to exposure times of 50.45 minutes for PDS 70 and 15.24 minutes for HD 123991.

The data were reduced using version 1.11.3 of the `JWST` pipeline², from the `uncal` data format. We use the default `calwebb_detector1` stage 1 pipeline and `calwebb_image2` stage 2 pipeline. Note that we do not use the `charge_migration` ³ step (Goudfrooij et al. 2024), that was designed to minimize the impact of the detector brighter-fatter effect (BFE). The `charge_migration` algorithm discards all data in each pixel above a set signal threshold, along with the rest of the data in the four directly adjacent neighbors. This strategy is not optimal for AMI data because, as we show in Appendix B, and has been shown in other works (e.g., Argyriou et al. 2023), charge bleeding from a bright pixel, into its neighbors, affects not only the four adjacent pixels, but also the four pixels along the diagonals, albeit somewhat less. Additionally, considering only the brightness of individual pixels is not the optimal threshold criteria because the BFE depends on the contrasts between pixels (e.g., Plazas et al. 2017). Due to the fine structure in the AMI PSF, that is somewhat undersampled at $4.8 \mu\text{m}$ with the NIRISS plate scale of ~ 66 mas, there are many parts of the PSF with large contrasts between neighboring pixels. The current pipeline BFE mitigation algorithm, therefore, is not useful for correcting AMI data. A modification to the existing pipeline, beyond the scope of this work, could be to base the

² <https://github.com/spacetelescope/jwst>

³ named `undersampling_correction` in the 1.11.3 version of the pipeline that we used

threshold on the contrast between adjacent and diagonal neighboring pixels.

We investigate the effect of the BFE on the data (see Appendix B for details), as it has been shown to be the limiting noise floor for AMI observations (Sivaramakrishnan et al. 2023; Kammerer et al. 2023; Ray et al. 2023; Sallum et al. 2023b). Based on our analysis, and to minimize the effect of the BFE on the calculated squared visibilities and closure phases, we discard all groups beyond where the sum of the central 3×3 pixels of the PSF is above 30,000 data number (DN), or $\sim 48,000$ electrons, in the linearized ramp-level data. We use this cutoff, as opposed to the intensity in the central pixel, because it is more robust against changes in PSF centering. This constraint corresponds to an apparent systematic change in the calculated rate in the central pixel of $\sim 1\%$, and minimal bleeding into surrounding pixels (Appendix B, Figure 10). We note that this loss in signal biases our measured contrasts by significantly less than 1% , due to the central pixel accounting for $\sim 1\%$ of the total signal in the PSF. This can be seen in Figure 1, which presents the mean PDS 70 image-plane data using only the first 28 groups. We also note that this BFE mitigation method is only possible because PDS 70 and HD 123991 are relatively faint, such that we have at least 10 groups before a peak signal level of ~ 5800 DN. With fewer groups, the data is likely to be dominated by the $1/f$ noise seen in the NIRISS detector (e.g., Sallum et al. 2023b). For PDS 70 we are therefore limited to 28 out of the total 96 groups, while for HD 123991 we are limited to 10 out of the total 29 groups.

We correct bad-pixels that were flagged by the pipeline by finding the pixel value that minimizes the power outside of the Fourier support of the AMI mask (Ireland 2013). We also perform sub-pixel centering of the data using a Fourier-based shift, by finding the position that minimizes the absolute value of the phase calculated from the mean of the cleaned data (Kammerer et al. 2019).

The background star near PDS 70 that was originally observed by Riaud et al. (2006), and confirmed to be a background star by Hashimoto et al. (2012), is at the edge of the SUB80 array, at a separation of ~ 2.5 arc seconds (as) from PDS 70 A. This is outside of the interferometric field-of-view, set by the shortest baseline, but the signal will still contaminate all baselines. To minimize the contribution to the calculated interferometric observables, a super-Gaussian window ($e^{-(r/\sigma)^4}$), with $\sigma = 30$ pixels, is applied to both the PDS 70 data and the HD 123991 data.

We calculate the squared visibilities, V^2 , and closure phases, of PDS 70 and calibrator, HD 123991, using

amical (Soulain et al. 2020; Soulain & Robert C. M. T. 2023). We also compute the statistical uncertainties (i.e. the standard error of the mean) of these quantities across integrations. The interferometric observables are calibrated, to remove the instrumental bias, by dividing the V^2 of PDS 70 by the V^2 of HD 123991. Similarly, the closure phases are calibrated by subtracting the closure phases of HD 123991 from those of PDS 70.

3. METHODS

Due to the interferometric nature of the data, we construct a model to jointly fit for flux from the star, extended disk emission, and the two known planets. This is required because the signal from all components is entangled and thus cannot be measured independently. We model the star and the two planets as delta functions, with their analytic Fourier transform given by

$$V_{*,b,c}(u, v) = I_* + I_b e^{-i2\pi(ux_b + vy_b)} + I_c e^{-i2\pi(ux_c + vy_c)}, \quad (1)$$

where I_* is the brightness of the star, I_b is the brightness of planet b, and I_c is the brightness of planet c. Additionally, x_b , y_b , x_c and y_c denote the x and y offset of planets b and c relative to the star (which is fixed at the phase center), and u and v are the baseline coordinates in the Fourier domain, in units of wavelength.

To model the extended disk emission, we use a simple geometrical model, as was used to successfully reconstruct the extended emission of LkCa 15, in the near infrared, with ground based AMI (Blakely et al. 2022). A simple model is sufficient due to the sparsity of the data, and the fact that the dominant signal is expected to be from the forward scattering peak of the disk. To construct this model, we assume that all of the disk signal that we are observing is optically thick emission from the disk surface, in a similar manner to the procedure used by Stolker et al. (2016) and Sissa et al. (2018). We describe the height of the surface of the disk using a power law profile, given by

$$z = H_{100} \left(\frac{\sqrt{x^2 + y^2}}{100\text{au}} \right)^\beta, \quad (2)$$

where x and y are the potentially rotated and/or inclined coordinates of the disk mid-plane, in units of au, H_{100} is the aspect ratio at 100 au (~ 0.9 arc seconds), and β is the flaring angle. To project this geometry into the plane of the sky, we define r to be the apparent distance from the star to the disk surface, given an observed inclination angle, i , relative to the plane of the sky,

$$r = \sqrt{x^2 + (y + z \sin(i))^2 + z^2}. \quad (3)$$

We describe the radial brightness distribution as a skewed Gaussian projected onto the flared disk geometry, given by $I_{d_1}(r) \cdot I_{d_2}(r)$, where $I_{d_1}(r)$ is defined as

$$I_{d_1}(r) = \exp\left(-\frac{(r - r_0)^2}{2\sigma_r^2}\right), \quad (4)$$

and $I_{d_2}(r)$ is

$$I_{d_2}(r) = \frac{1}{2} \left(1 + \operatorname{erf} \left(\alpha \frac{(r - r_0)}{\sqrt{2}\sigma_r} \right) \right), \quad (5)$$

where r_0 describes the location of the peak of the disk brightness, σ_r describes the radial extent of the disk emission and α describes the degree to which the inner edge of the disk is truncated.

The azimuthal brightness distribution is a sum of an axisymmetric component and an asymmetric component described by the Henyey-Greenstein scattering phase function (Henyey & Greenstein 1941)

$$I_{d_3}(\theta) = \frac{1 - g^2}{4\pi(1 + g^2 - 2g \cos(\theta - \theta_0))^{3/2}}, \quad (6)$$

where g is the scattering parameter, a free parameter constrained to be between 0 (isotropic scattering) and 1 (forward scattering), and θ_0 is the azimuthal location of the scattering peak, which is fixed to the near side of the disk.

Combining Equations 2 through 6, the full disk model is given by

$$I_d(r, \theta) = (A_a I_{d_3}(\theta) + A_s) I_{d_1}(r) I_{d_2}(r), \quad (7)$$

where A_a and A_s control the brightness of the asymmetric and symmetric components, respectively. The Fourier transform of Equation 7 is calculated using the one-sided discrete Fourier transform (DFT) as implemented in XARA (Martinache 2010, 2013; Martinache et al. 2020), to exactly compute the DFT at the baseline coordinates of the NIRISS aperture mask baselines.

Finally, any over-resolved emission is included in the model using a single free parameter I_o , that contributes additional flux to the normalization of the visibilities. The full model consists of the sum of Equation 1 and the DFT of Equation 7, normalized by the total flux of the model. The complex visibilities of this 17 parameter model are given by

$$V_m = \frac{\mathcal{F}\{I_d\} + V_{*,b,c}}{\Sigma I_d + I_* + I_b + I_c + I_o}. \quad (8)$$

We calculate the closure phase of the model by summing the phase measured between baselines that form a (closure) triangle, for all 35 triplets of holes in the aperture mask, corresponding to 15 independent measurements. Squared visibilities are the squared amplitude of

the complex visibilities, corresponding to each of the 21 baselines formed by pairs of mask holes.

We follow the general procedure used by [Blakely et al. \(2022\)](#) and [Sallum et al. \(2023a\)](#) of fitting geometrical models to the squared visibilities and closure phases calculated from AMI data. Our log-likelihood is the sum of an unnormalized Gaussian log-likelihood for both the closure phases and squared visibilities. For the closure phases, the uncertainties are simply the statistical uncertainties, calculated across integrations. However, for the squared visibilities, to account for a measurable drift at each baseline, observed as the signal level increases, even at low flux levels, an estimated systematic error budget of 1% is added in quadrature with the statistical uncertainties. We estimate this 1% systematic on the squared visibilities by comparing the calculated squared visibilities for PDS 70 and HD 123991 for all signal levels (we show the evolution of pixel intensities in [Appendix B, Figure 10](#)). We observe a drift from group 1 up to our cutoff signal level (groups 28 and 10 for PDS 70 and HD 123991, respectively) that is inconsistent with the calculated statistical uncertainties. We find that the difference in the evolution of the squared visibilities between PDS 70 and HD 123991 is $\sim 1\%$ at the cutoff signal. We do not include a similar systematic for the closure phases because the evolution we see for increasing signal level is largely consistent with the calculated statistical uncertainties.

We use a Bayesian modelling approach to measure the locations and contrasts of PDS 70 b and c, as well as our model disk parameters. We estimate our model posterior using dynamic nested sampling ([Higson et al. 2018](#)), with `dynesty` ([Speagle 2020](#); [Koposov et al. 2023](#)). We use uniform priors on the contrasts of both planets, between 0 and 10 Δmag . We also use uniform priors on the locations of PDS 70 b and c and then we test this result against a model that uses tightly constrained Gaussian priors, henceforth referred to as GRAVITY priors, based on the planets predicted locations from [Wang et al. \(2021b\)](#), made using VLTI/GRAVITY astrometry. The planet location priors are given in [Table 3](#), in [Appendix A](#). We use priors on the the disk geometry from [Keppler et al. \(2018\)](#) and [Keppler et al. \(2019\)](#), that are described in [Appendix A](#).

We note that there are limitations to our joint model fitting approach due to its necessarily simple nature. This means that, despite the ability of our joint-modelling approach to measure the correlations between the planet and disk parameters, the planet parameter uncertainties derived from our nested sampling fitting do not capture the full uncertainties in the physical parameters that we are trying to measure. To provide

conservative estimates on the uncertainties of our derived parameters for PDS 70 b and c, we estimate a systematic uncertainty on their separations, position angles and contrasts. We use an injection/recovery approach similar to what is used by [Stolker et al. \(2024\)](#). Because of the non-linearity of closure phases (especially in the moderate contrast regime, where the visibility amplitudes are not ~ 1), we mimic the injection of point sources into the data by injecting a companion with a negative flux into the model complex visibilities before we calculate the model closure phase and squared visibilities. We inject the companion at the median separation and (negative) contrast of PDS 70 b and c found from our nested sampling fits at position angles between 0 and 360 degrees, in increments of 5 degrees. We recover the parameters using nested sampling for each case, while fixing the disk parameters to the median parameters from the original nested sampling fit. To estimate the systematic uncertainty on the planet parameters, we use the root-mean-square deviation of the median estimated parameters from the true parameters, at each position angle.

The mean parameters for the locations and contrasts of PDS 70 b and c, along with the standard deviation of the distribution calculated with nested sampling with the estimated systematic uncertainty added in quadrature are shown in [Table 1](#). For PDS 70 b, we estimate a systematic in the contrast of 0.08 mags, 3.4 mas in separation and 1.2 degrees in position angle. Only the contrast systematic has a significant contribution to our total error budget, compared to the uncertainties estimated with nested sampling ([Appendix A, Table 3](#)). For PDS 70 c, we find a contrast systematic of 0.08 mags, a separation systematic of 7.0 mas, and a position angle systematic of 0.8 degrees. Both the contrast and separation systematic uncertainties have a non-negligible contribution to the total error budget, indicating that there is some level of degeneracy between the disk signal and a companion with the contrast that we estimate for PDS 70 c that we are able to capture using this injection/recovery procedure.

To convert the measured contrasts to fluxes, we model the spectral energy distribution of the unresolved stellar plus inner disk emission using a power law, assuming that any spectral features over the range of the F480M filter ($\sim 4.6\text{-}5.0 \mu\text{m}$) are negligible, using the same approach as is done by [Stolker et al. \(2020a\)](#). We fit the power law, in log-log space, to 2MASS ([Skrutskie et al. 2006](#)) J, H and Ks as well as WISE ([Wright et al. 2010](#)) W1 and W2 magnitudes that we convert to fluxes using `species` ([Stolker et al. 2020b](#)). We employ nested sampling ([Skilling 2004](#)), using `dynesty`, to estimate the

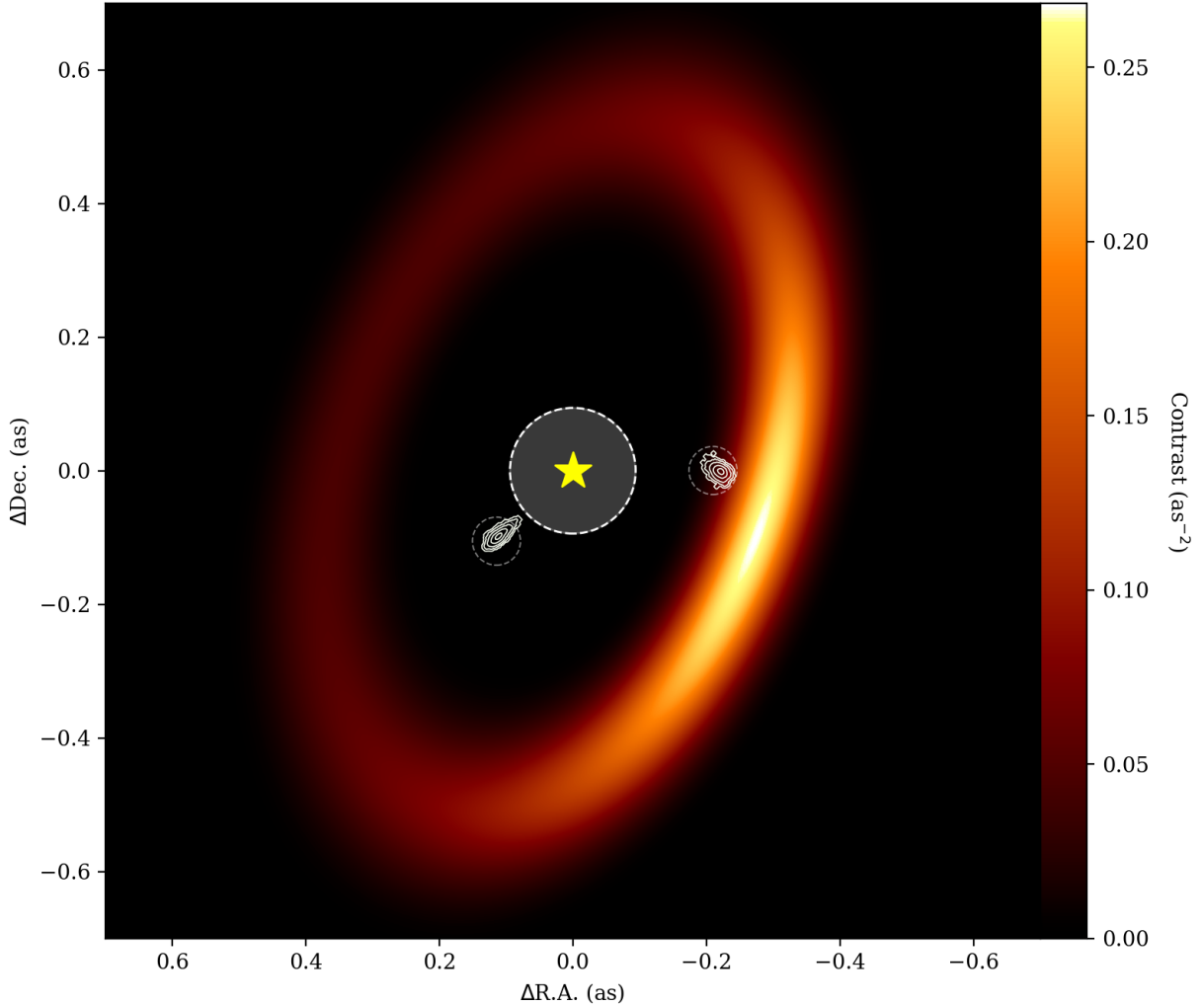


Figure 2. Geometrical model fit to the F480M closure phase and squared visibility data of PDS 70 (images), using uniform priors on the positions of PDS 70 b and c. With respect to the central source (yellow star), PDS 70 b is to the south-east while PDS 70 c is directly west. The white contours denote the 1, 2, 3, 4 and 5 σ contours of the marginalized posterior of the positions of PDS 70 b and c. The two grey dashed circles are centered on the predicted locations of the planets at the time of the observations (Wang et al. 2021b) from *wheretheplanet* (Wang et al. 2021a). We mask the central region to denote the inner working angle of $\sim 0.5\lambda/B = 94$ mas, the diffraction limit of the data.

posterior of the power-law model. To account for the outer disk flux, which we measure in our fits to be $\sim 4\%$ of the stellar flux, we scale the model spectrum by 0.96, finding a stellar magnitude of 7.56 ± 0.02 , in F480M. To convert the measured contrasts of the planets to physical units we integrate the model spectrum across the F480M filter transmission profile. To estimate the uncertainties on the derived fluxes we do this for all combinations of the planet contrast posterior samples and 500 randomly drawn samples from the power law model posterior, and calculate confidence intervals from this distribution.

4. RESULTS

4.1. Derived Planet Parameters

Figure 2 shows the two planet plus disk model generated from the median parameters from the uniform planet location model posterior. The 1, 2, 3, 4 and 5 σ contours from the marginalized posterior of the planet locations are shown by the white contours. A comparison of the model squared visibilities and closure phases to the data is given in Figure 3, showing that the model provides an excellent fit. Furthermore, the measured positions of both PDS 70 b and c are consistent with VLTI/GRAVITY predictions from Wang et al. (2021b), which are shown by the dashed grey circles in Figure 2.

Table 1 summarizes the derived planet parameters, from both of the models. The disk model parameters

Table 1. PDS 70 b and c parameters

	Separation (mas)	Position Angle ($^{\circ}$)	Contrast (Δmag)	Flux ($\text{W m}^{-2} \mu\text{m}^{-1}$)	SNR
PDS 70 b	147.8 ± 8.2	131.5 ± 1.6	5.83 ± 0.10	$8.75 \pm 0.82 \times 10^{-17}$	21.1
PDS 70 c	221.1 ± 8.7	269.6 ± 1.4	6.48 ± 0.13	$4.83 \pm 0.58 \times 10^{-17}$	10.6

Notes: We report the mean and the standard deviation of the marginalized posteriors, with the systematic uncertainties estimated from the injection/recovery added in quadrature with the nested sampling uncertainties. The SNR is defined here as the mean of the contrast posterior samples divided by its standard deviation from nested sampling only (displayed in Appendix A, Table 3).

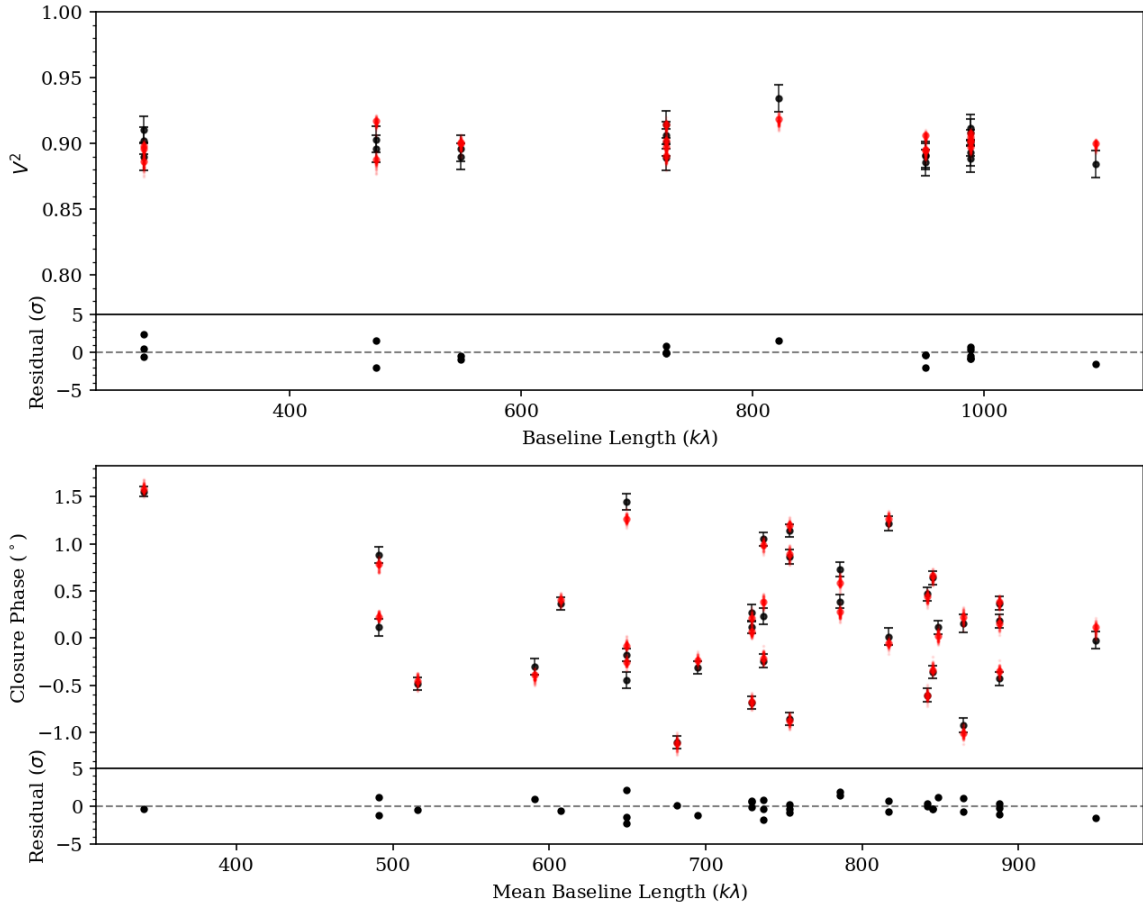


Figure 3. Squared visibility data, black, with the model squared visibilities plotted in red (top) and the closure phase data, black, with the model closure phases shown in red (bottom), for the two point source (with uniform priors on the planet locations) plus disk geometrical model fit to the F480M data. For both panels, the large red circles denote the values calculated with the median parameter model, and 100 random posterior samples are denoted by the small, transparent red points. The noise normalized residuals are shown below both panels.

are listed in Table 2 in Appendix A. We find that both planets are found at a high signal-to-noise (SNR) ratio, in locations that are consistent between the uniform prior and tightly constrained Gaussian prior models. We also find that the measured contrasts of the planets are consistent for the uniform prior and GRAVITY prior models, with nearly identical contrasts derived for PDS 70 b, and a small difference for PDS 70 c, at the $\sim 1\sigma$ level.

Figure 4 shows a corner plot of the planet parameters from the uniform prior model, along with a correlation matrix of all of the model parameters. We note that there are correlations between the parameters of both planets. Notably, there is a moderate anti-correlation between the separation and the contrast of PDS 70 c, which may explain the slight discrepancy between the derived contrast of PDS 70 c between the uniform prior model and the GRAVITY prior model. From the correlation matrix, there are no strong correlations between the disk parameters and the planet contrasts, indicating that the disk model has a minimal effect on the measured contrasts.

4.2. Residual Signal and Contrast Limits

We compute an SNR map, shown in Figure 5, made by dividing the best fit point source binary contrast to the residual closure phase signal by its associated uncertainty fitting, using our new python package `drpangloss`⁴. `drpangloss` provides similar capabilities to the packages CANDID (Gallenne et al. 2015) and `fouriever` (Kammerer et al. 2023) but is written using JAX to provide just-in-time (JIT) compilation, GPU compatibility and auto-differentiation.

Because closure phases are non-linear, we calculate the complex visibilities of the uniform prior model, using the median of the marginalized posterior for all parameters, and add this to our binary model visibilities before calculating the model closure phases. Each cell in the grid shows the best fit contrast divided by the uncertainty in the contrast calculated using the Laplace approximation (Tierney & Kadane 1986), assuming the uncertainties are Gaussian. We clearly see that there is residual emission at an SNR of ~ 4 , to the south-west of PDS 70 A and very close to the inner working angle of 94 mas, that is not fully captured by our two planet plus disk model. To assess the nature of the signal that we observe, we use nested sampling to fit a star plus planet model to the residual closure phases and find a contrast of $7.6_{-1.3}^{+0.6}$ magnitudes, a separation of 100_{-42}^{+45}

mas and a position angle of 207_{-10}^{+11} degrees. The position angle of the signal is well constrained, however, there is a strong anti-correlation between the separation and contrast, which is expected for a high contrast source near the diffraction limit. Interestingly, the position angle of the observed signal is not consistent with forward scattering from an inner disk that has the same geometry as the outer disk. However, due to the unconstrained nature of the separation of the emission it is unclear whether the signal is due to compact emission or an inner disk feature.

To assess the limits that we are able to place on the presence of additional planets in the system, we calculate a 5σ contrast curve, from the residual closure phase signal of the uniform prior model. We use the approach described above to fit to the residual closure phase signal, and calculate the contrast curve using the Absil method (Absil et al. 2011; Gallenne et al. 2015), as is implemented in `drpangloss`. We note that the Absil method is a standard approach to measuring contrast limits for interferometric data, however, it is based on a model comparison between a single star model and a binary model, and calculates the contrast at which the binary model deviates by a certain probability from the single star model (Kammerer et al. 2023). In this work, we wish to calculate an upper limit on the flux, at each location, in our field-of-view. To measure Bayesian upper limits, we adapt the method presented by Ruffio et al. (2018) to interferometric data. We first, calculate a grid of likelihoods for a binary model at fixed R.A. and Dec. locations for a range of contrasts. We next, use the maximum likelihood point in each grid cell to initialize gradient descent, using the BFGS algorithm (Broyden 1970; Fletcher 1970; Goldfarb 1970; Shanno 1970), to find the contrast that maximizes the likelihood. We use the calculated contrast in each cell, along with the Laplace approximation to calculate the uncertainty in the calculated contrast at each R.A. and Dec. point. Finally, we plug the calculated contrasts, uncertainties and a 99.999971% cutoff probability into Equation 8 in Ruffio et al. (2018), to calculate the $5\sigma_{eq}$ upper limit at each point in our field of view, which azimuthally average over to generate a contrast curve. We henceforth refer to this method as the Ruffio method.

The derived 5σ contrast/upper limit curves, and their 1σ uncertainties, calculated using the Absil and Ruffio methods, are shown in Figure 6. We reach a contrast upper limit of ~ 7.5 Δ mag, which is reasonably consistent with the expected photon noise limit of ~ 7.8 , given by Equation 10 by Sivaramakrishnan et al. (2023). The contours show the 1, 2 and 3 σ confidence intervals on

⁴ <https://github.com/benjaminpope/drpangloss>

the contrast and the separation for PDS 70 b and c calculated from the uniform prior model posterior.

We also calculate a $5\sigma_{eq}$ upper limit on any flux at the reported position of the planet candidate PDS 70 d from Christiaens et al. (2024) (sep. = 115.2 mas, P.A. = 291.8°), as our observations are only separated by 12 days. We first calculate the contrast posterior distribution using *dynesty*, with uniform priors on the contrast, from -1 to 1. We find a mean contrast of $-5.3 \times 10^{-4} \pm 1.9 \times 10^{-4}$. To convert this measured contrast to an upper limit, we use Equation 8 by Ruffio et al. (2018), with the measured mean, standard deviation and a cutoff probability of 99.999971%, which is equivalent to a 5σ upper limit, with a positivity prior on the contrast. From this, we calculate a $5\sigma_{eq}$ upper limit of 7.56 mag, corresponding to a flux of $1.76 \times 10^{-17} \text{ W m}^{-2} \mu\text{m}^{-1}$. We also calculate the $5\sigma_{eq}$ upper limit using the Laplace approximation and find an upper limit of 7.57 mag, consistent with the nested sampling result within <1%.

4.3. SED Fitting

We fit the the available data points of both protoplanets including the new NIRISS/AMI F480M measurement. For planet b, we use the SPHERE/IFS spectrum and SPHERE/IRDIS photometries from Müller et al. (2018), the VLTI/GRAVITY spectrum from Wang et al. (2021b), the VLT/NaCo photometries at 3–5 μm from Stolker et al. (2020a), and the F187N and F480M NIRCcam measurements from Christiaens et al. (2024). For planet c, we consider the SPHERE/IRDIS and VLT/NaCo photometries from Stolker et al. (2020a), the SPHERE/IFS and VLTI/GRAVITY from Wang et al. (2021b), and the F187N and F480M NIRCcam measurements from Christiaens et al. (2024).

Given the best-fit presented by Wang et al. (2021b), we use the Drift-PHOENIX models (Woitke & Helling 2003, 2004; Helling & Woitke 2006; Helling et al. 2008) to describe the atmospheric emission from the protoplanets. Following Wang et al. (2021b), we do not apply any correction for extinction. The parameter space is explored using *pymultinest* (Buchner et al. 2014), employing 1000 live points. For both planets, we first fit the available data without including any CPD contribution. We then include a CPD contribution in the form of a single temperature blackbody. Blackbody emission has been shown to be the simplest model able to describe well the circumplanetary disk emission of GQ Lup B up to 11.7 μm (Cugno et al. 2024). Although a blackbody is a simple model and it is not the only possible solution to characterize CPD emission, more complex models would not provide useful information as the CPD contribution

is mostly determined by the F480M photometry. The model parameters for both PDS 70 b and c are shown in Section A.4.

For planet b, the best fit without a CPD component is reported by the green solid line in Figure 7. The spectrum reproduces well the IFS spectrum, the SPHERE *H* band photometries, and the F187N measurement obtained with NIRCcam. However, the first half of the GRAVITY spectrum is underestimated, while the second appears to be overestimated. Finally, at $\lambda > 3 \mu\text{m}$, almost none of the datapoints appear to agree within 1σ with the best-fit model, with the exception of the NIRCcam F480M photometry, which has a very large uncertainty. When including the CPD contribution, the second half of the GRAVITY spectrum is better reproduced, while at longer wavelengths the predicted flux is closer to the measurements (see orange dashed line in Figure 7). In terms of planet model parameters, the presence of MIR excess emission in the modeling suggests a hotter and smaller planet. The reduced chi square is 0.9 for the extincted Drift-PHOENIX model alone and 0.53 for the extincted Drift-PHOENIX+blackbody model. Additionally, the Bayes factor comparing the blackbody model to the no blackbody model is 1.6×10^8 . Hence, the presence of the blackbody provides a better description of the observations.

The results for planet c are displayed in Figure 8. As reported by Christiaens et al. (2024), the F187N shows an excess emission, possibly due to Pa α emission. The blue region of the GRAVITY spectrum does not agree with the fit, and the *L'* measurement is off by almost 2σ . Also, our NIRISS/AMI F480M measurement is clearly at odds with respect to the green solid line model fit, which does not include a CPD component. The spectrum of the best model once including the CPD presents a lower *L'* flux, consistent with the NaCo measurement. Furthermore, the CPD contribution passes right in between the F480M measurements from NIRCcam and NIRISS. The reduced chi squared for these fits are 0.55 and 0.52 respectively, and the Bayes factor in favour of the model including the blackbody is 5.6, suggesting moderate support for including the blackbody component. Furthermore, assuming that the NIRISS/AMI long-wavelength measurement is less biased, weighting it more strongly would obtain a warmer/larger CPD contribution.

5. DISCUSSION

5.1. PDS b and c F480M Photometry

For PDS 70 b, and the uniform prior model, we find a contrast of $4.67 \pm 0.43 \times 10^{-3}$ (5.83 ± 0.10 mags). Sim-

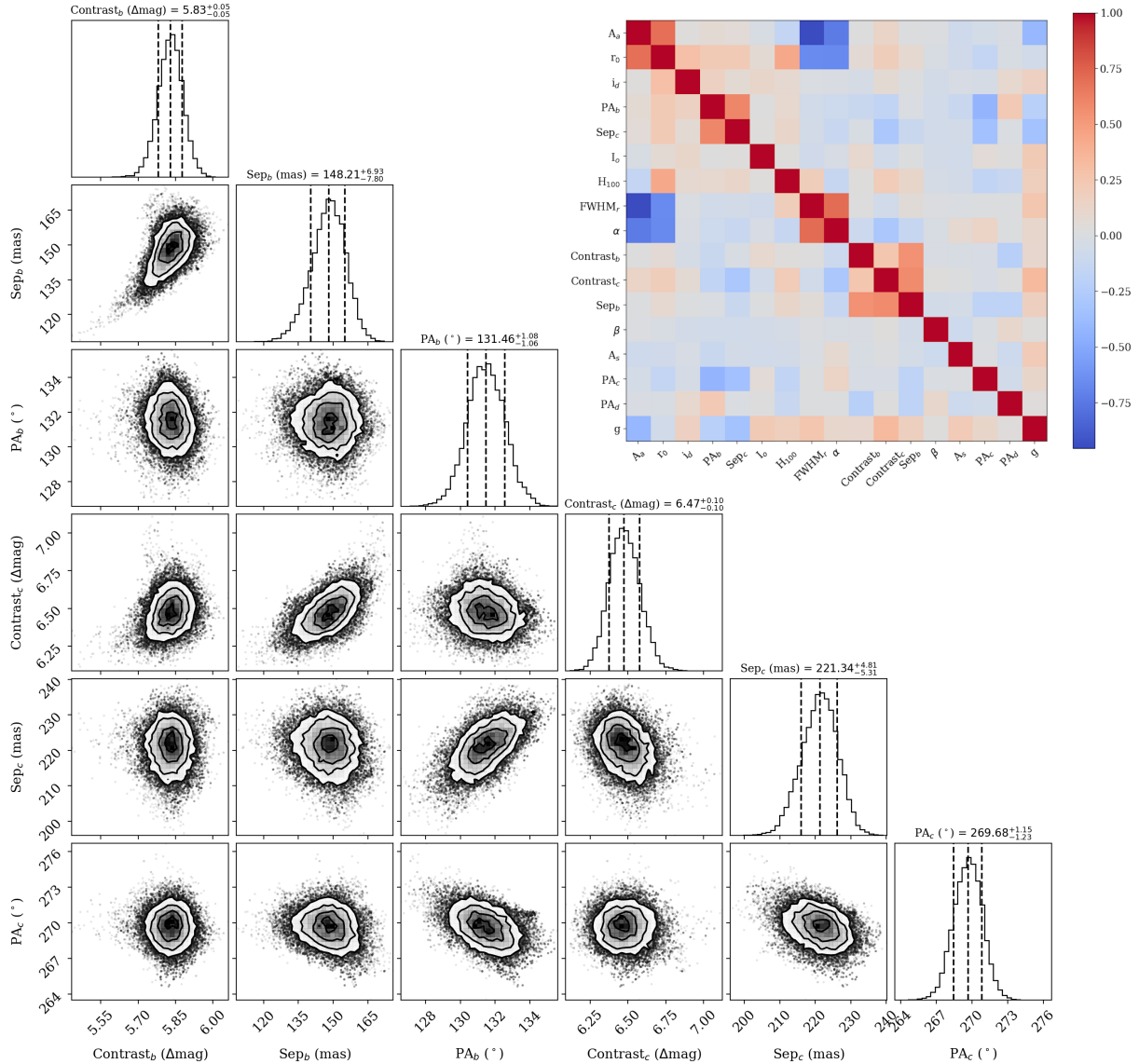


Figure 4. Corner plot showing the 1D and 2D marginalized posteriors of the companion parameters from the joint two point source plus geometrical model fit to the F480M squared visibilities and closure phases, with uniform priors on the planet locations. The top right figure shows the correlation matrix of all of the model parameters.

ilarly, for PDS 70 c, and the uniform prior model, we find a contrast of $2.58 \pm 0.31 \times 10^{-3}$ (6.48 ± 0.13 mags). While our result for PDS 70 b is consistent with the NIRCcam F480M results of $3.44 \pm 1.50 \times 10^{-3}$ published by Christiaens et al. (2024), and reasonably consistent with the M' contrast of 6.15 ± 0.27 mags published by Stolker et al. (2020a), the PDS 70 c value is inconsistent with the NIRCcam F480M results of $1.47 \pm 0.30 \times 10^{-3}$, at roughly the 3σ level.

There are several possible reasons for the PDS 70 c discrepancy between NIRCcam and NIRISS/AMI. It is possible that the contrasts published by Christiaens et al. are systematically underestimated due to self/over subtraction, as a result of the small roll angle of ~ 5 degrees

between their two observations. Another possibility for an underestimated brightness of PDS 70 c could be due to over subtraction of the spatially coincident disk. Christiaens et al. use a radiative transfer model based on models published by Portilla-Revelo et al. (2022) and Portilla-Revelo et al. (2023), that were originally fit to ALMA data and $1.25 \mu\text{m}$ polarized VLT/SPHERE data of PDS 70. These models were iterated on by fitting for the minimum grain size and settling parameters to less than half of the forward scattering side of the disk, in F480M. This tightly constrained fitting approach could lead to biased results that do not adequately reproduce the disk emission at the location of PDS 70 c. Specifically, an incorrect estimation of the scattering phase

function will significantly impact the PDS 70 c measured contrast.

Separating out the disk emission is less of an issue for the interferometric data set despite the simple disk model employed, using a symmetric, optically thick disk component plus the asymmetric Henyey-Greenstein scattering phase function. The signals of the disk and the planet in Fourier space are well separated and thus we can disentangle the asymmetric contributions from the forward scattering peak of the disk, and PDS 70 c, offset by ~ 20 degrees, due to the majority of our likelihood being from the closure phases (the squared visibilities are nearly flat at a signal level of ~ 0.90 , Figure 3). Furthermore, our joint modelling of the planet and disk parameters allows us to measure the correlations between the parameters of both planets and the disk, which are shown by the correlation matrix in the top right of Figure 4. Notably for the contrast of PDS 70 c, there is a moderate correlation with g , the scattering parameter (more forward scattering leads to less emission), a strong correlation with the separation of PDS 70 b (larger separation leads to less emission), a moderate anti-correlation with α , the disk inner-edge truncation parameter and a moderate anti-correlation with its own separation from the star (plus unresolved inner disk emission).

We note that these correlations, between the contrast of PDS 70 c and the disk model parameters, are small compared to the correlation between the contrast of PDS 70 c and the separation of PDS 70 b, which is evident in Figure 4. This means a larger separation of PDS 70 b would correspond to a fainter contrast of PDS 70 c. To assess the impact of this correlation, we calculate the contrast of PDS 70 c using only posterior samples within 3σ of the predicted location of PDS 70 c from the orbit fitting presented in Wang et al. (2021b). We find a contrast of 6.53 ± 0.12 mags, consistent with our value of 6.48 ± 0.13 mags, calculated using the full posterior. As an additional test to explore the impact of the scattering phase function profile, we briefly explored other simple parametric scattering phase functions. We tested an azimuthal Gaussian profile and the sum of an azimuthal Gaussian profile and the Henyey-Greenstein scattering phase function. We repeated the model fitting procedure described in Section 3, using uniform priors on the planet locations, and found contrasts for PDS 70 b and c that were nearly identical to the results reported in Table 1 (and Table 3, in Appendix A) for both models.

As another test, we briefly explored including an inner disk component in our model, with its geometry fixed to that of the outer disk. We tested symmetric models as well as models that included skewed emission in

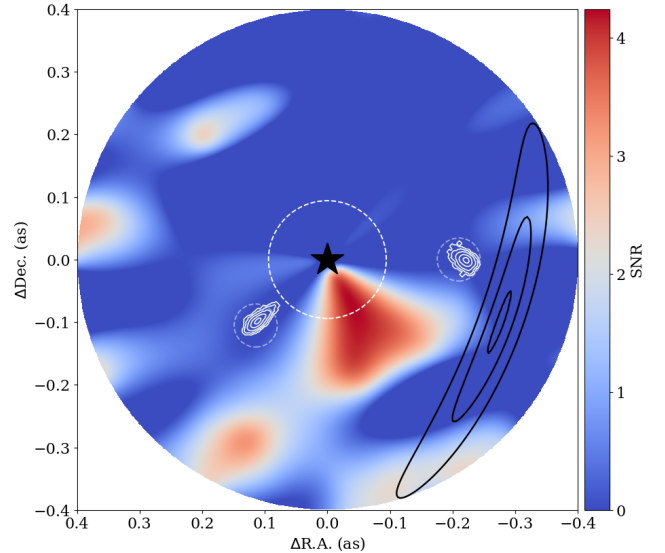


Figure 5. Point source model SNR map calculated from the closure phase residuals from the two point sources plus geometrical model fit that used uniform priors on the location of PDS 70 b and c. The white contours denote the 1, 2, 3, 4 and 5 σ contours from the posterior calculated with nested sampling. The grey dashed lines denote the predicted locations of PDS 70 b and c at the time of the observations (Wang et al. 2021b,a). The black star denotes the position of the star. The black contours denote the forward scattering side of the outer disk in our model. As in Figure 2, the white dashed circle denotes the diffraction limit of the data.

the forward scattering direction. We found that symmetric models did not noticeably improve the fit. For the skewed models, we found that the fit did somewhat improve, for a large, bright, extended inner disk model, however, we saw significant correlations between the inner disk and the planet location parameters. Such a bright and large inner disk is inconsistent with the size and mass of the inner disk that has been inferred from SED fitting (e.g., Gaidos et al. 2024). Additionally, the planet contrasts that we found from these tests were all consistent with the planets plus outer disk only model, well within 1σ of the contrasts that we report in Table 3. Given these points, as well as the fact that the inner disk is marginally resolved, if at all, and that it possibly has a complicated morphology (Mesa et al. 2019; Casassus & Cárcamo 2022), not well captured by a geometrical model, we decided not to further explore an inner disk model component.

5.2. Contrast Limits and the Nature of the Signal Seen in the Residuals

The residual signal shown in Figure 5, is in a direction significantly offset from the expected forward scattering direction of the inner disk. This indicates that what we

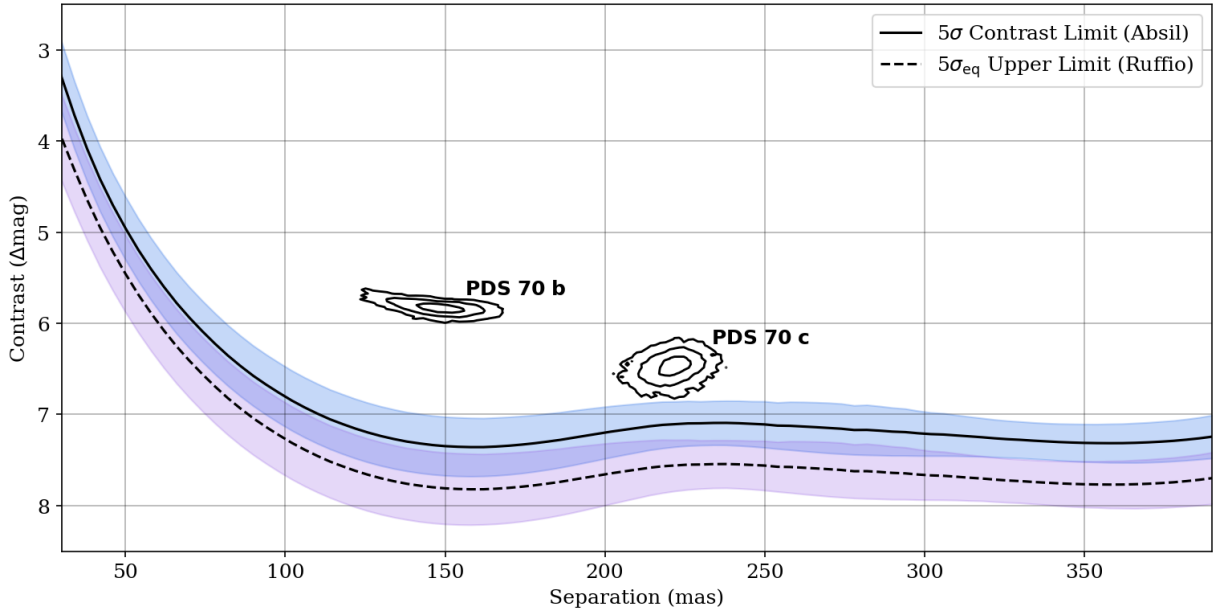


Figure 6. Mean contrast curves calculated from the residuals of the geometrical model plus two point source fit, that used uniform priors on the planet locations. The solid line denotes the 5σ contrast curve calculated using the Absil method. The dashed line denotes the $5\sigma_{eq}$ upper limit calculated using the Ruffio method. The coloured regions denote one standard deviation from the mean. The 1, 2, and 3 σ confidence intervals of the planet contrast/separation, calculated from the nested sampling posterior of the model fit using uniform priors on the planet locations, are denoted by the black contours. We note that, for the signal depth of our data, the expected contrast limit for photon noise dominated data is ~ 7.8 , from by Equation 10 in Sivaramakrishnan et al. (2023).

observe is not due to a simple inner disk structure, and may hint at a complex inner disk morphology such as a spiral or clumpy features, as has been suggested by Casassus & Cárcamo (2022), from ALMA observations in the mm, and by Mesa et al. (2019) from near-infrared observations with VLT/SPHERE. It is also possible that the asymmetry we observe is related to the larger separation, ~ 180 mas, ALMA compact emission seen by Balsalobre-Ruza et al. (2023), as it is at very similar position angle. It might even highlight extended emission from an accretion stream between PDS 70 b and c, tentatively detected by Christiaens et al. (2024). Another scenario is that the signal we observe is due to an additional planet interior to the orbit of PDS 70 b. To distinguish between these many scenarios, follow-up observations, at similar wavelengths, will be necessary with the James Webb Interferometer. Analysing follow-up data using an approach similar to Thompson et al. (2023a), using `Octofitter`⁵ (Thompson et al. 2023b), would allow for a robust detection of any orbital motion, even with low significance detections or non-detections at individual epochs.

⁵ <https://seffal.github.io/Octofitter.jl/dev/>

Additionally, it is clear from our SNR maps (Figure 5), and our contrast upper limit of 7.56 mags derived in Section 4, that we do not detect a signal (to the north-west of PDS 70 A, at a P.A. $\approx 291.8^\circ$) consistent with the point-like feature (PLF) seen by Mesa et al. (2019)/PDS 70 d seen by Christiaens et al. (2024), detected at shorter wavelengths. This indicates that if the signal is a planet, it likely traces bright scattered light emission from a potential planetary envelope instead of indicating another warm source like both PDS 70 b and c. This scenario would be similar to the protoplanet candidate HD 169142 b (Hammond et al. 2023).

Our contrast upper limits, shown in Figure 6, are the deepest limits on additional point source emission within ~ 250 mas in the disk gap of PDS 70, at $4.8 \mu\text{m}$. This clearly demonstrates the power of the James Webb Interferometer at probing small angular scales compared with direct imaging that achieves significantly better contrasts at larger separations, as is seen by Christiaens et al. (2024).

6. CONCLUSIONS

In this work, we present James Webb Interferometer observations of PDS 70 with the NIRISS F480M filter, the first space-based interferometric observations of this system. Using a joint model fitting approach to simul-

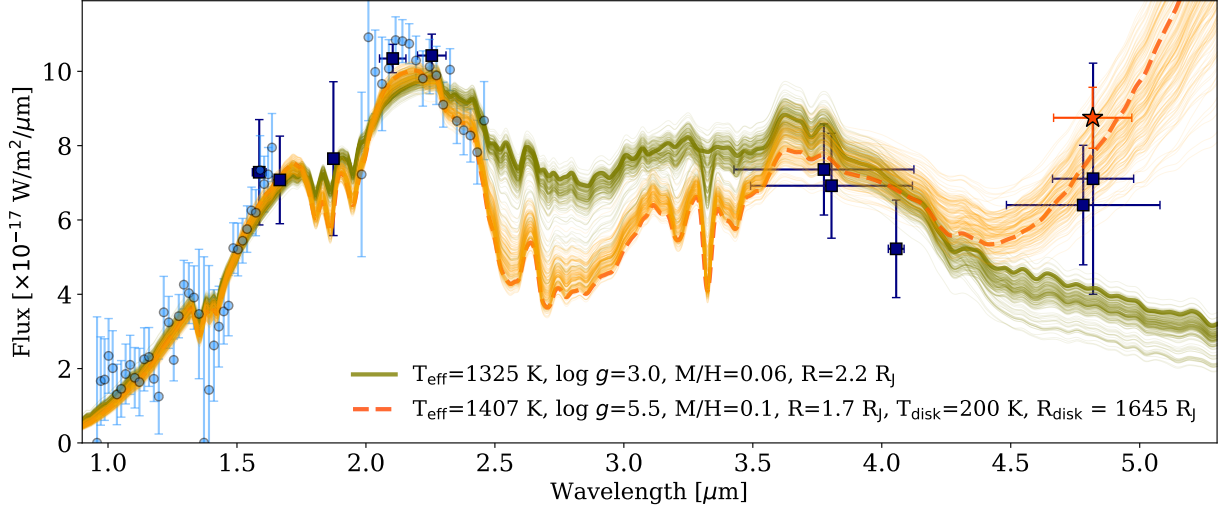


Figure 7. Spectral fit of PDS70 b using Drift-PHOENIX models with (dashed orange line) and without (solid green line) contribution from a CPD. Blue circles represent the IFS and GRAVITY spectra, while the photometric datapoints are reported with a blue square. Horizontal errorbars represent the effective width of the filters. The red star shows the new NIRISS F480M measurement. The thick lines are the spectra obtained from the set of parameters providing the maximum likelihood, while the thin lines report 100 samples randomly drawn from the posterior distribution.

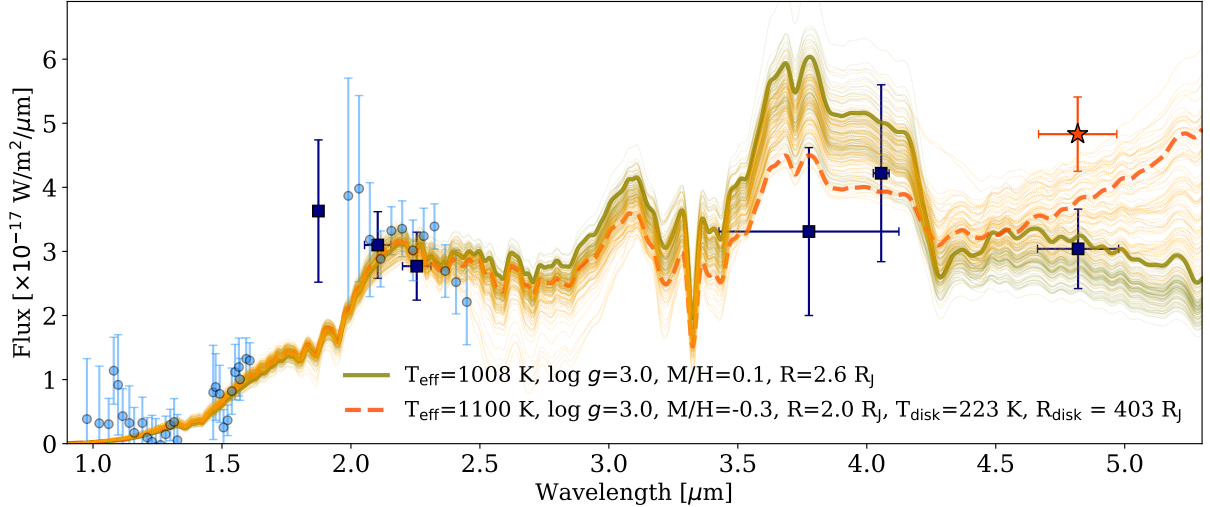


Figure 8. Same as Figure 7, for PDS 70 c.

taneously fit for star, disk, and planet emission, we re-detect the protoplanets PDS 70 b and c, and derive fluxes of both planets in this filter (Table 1). Additionally, we place the deepest constraints on additional planets within the disk gap of PDS 70 inside ~ 250 mas in F480M, and calculate an F480M upper limit on the flux of the candidate PDS 70 d. We also detect a new feature at an SNR of ~ 4 , to the south of PDS 70 A, whose nature is uncertain and will require follow-up observations to confirm.

Furthermore, our results show that NIRISS/AMI can reliably measure relative astrometry and contrasts of young planets in a part of parameter space (small separa-

rations and moderate to high contrasts) that is unique to this observing mode, and inaccessible to all other present facilities at $4.8 \mu\text{m}$. We demonstrate a NIRISS/AMI observing strategy for targets faint enough to acquire greater than ~ 10 groups up the ramp before the signal in the central 9 pixels reaches a total (linearized) value of 30,000 DN ($\sim 48,000$ electrons). We show that by using this stringent data selection criteria, we achieve nearly photon noise limited performance. For observing brighter targets, and to overcome the limitation of the sparsity of the NIRISS AMI uv-coverage, methods that are able to analyze the data directly in the image plane (or using the full extent of the Fourier "splodges")

will be necessary. A promising approach will be forward modelling of the full optical system and detector systematics (e.g., the brighter-fatter effect, $1/f$ noise) as is made possible with ∂ Lux (Desdoigts et al. 2023).

7. ACKNOWLEDGEMENTS

This work is based on observations made with the NASA/ESA/CSA James Webb Space Telescope. The data were obtained from the Mikulski Archive for Space Telescopes at the Space Telescope Science Institute, which is operated by the Association of Universities for Research in Astronomy, Inc., under NASA contract NAS 5-03127 for JWST. These observations are associated with program GTO 1242, and can be accessed via doi:10.17909/6qvy-zr60.

D.B. and D.J. acknowledge the support of the Natural Sciences and Engineering Research Council of Canada (NSERC). M.D.F. is supported by an NSF Astronomy and Astrophysics Postdoctoral Fellowship under award AST-2303911. J.S.-B. acknowledges the support received from the UNAM PAPIIT project IA 105023.

We acknowledge and respect the Lək^wəḡən (Songhees and Esquimalt) Peoples on whose territory the University of Victoria stands, and the Lək^wəḡən and WSÁNEĆ Peoples whose historical relationships with the land continue to this day.

BJSP acknowledges the traditional owners of the land on which the University of Queensland is situated, and PGT and LD would like to acknowledge the Gadiagal People of the Eora nation: upon whose unceded, sovereign, ancestral lands they works, and pays respect to their Ancestors and descendants, who continue cultural and spiritual connections to Country.

Software: JAX (Bradbury et al. 2018), NumPy (Harris et al. 2020), dynesty (Speagle 2020; Koposov et al. 2023), Astropy (Astropy Collaboration et al. 2013, 2018), Matplotlib (Hunter 2007), corner (Foreman-Mackey 2016), pymultinest (Buchner et al. 2014).

REFERENCES

- Abil, O., Le Bouquin, J. B., Berger, J. P., et al. 2011, A&A, 535, A68, doi: [10.1051/0004-6361/201117719](https://doi.org/10.1051/0004-6361/201117719)
- Argyriou, I., Lage, C., Rieke, G. H., et al. 2023, A&A, 680, A96, doi: [10.1051/0004-6361/202346490](https://doi.org/10.1051/0004-6361/202346490)
- Astropy Collaboration, Robitaille, T. P., Tollerud, E. J., et al. 2013, A&A, 558, A33, doi: [10.1051/0004-6361/201322068](https://doi.org/10.1051/0004-6361/201322068)
- Astropy Collaboration, Price-Whelan, A. M., Sipőcz, B. M., et al. 2018, AJ, 156, 123, doi: [10.3847/1538-3881/aabc4f](https://doi.org/10.3847/1538-3881/aabc4f)
- Balsobre-Ruza, O., de Gregorio-Monsalvo, I., Lillo-Box, J., et al. 2023, A&A, 675, A172, doi: [10.1051/0004-6361/202346493](https://doi.org/10.1051/0004-6361/202346493)
- Benisty, M., Bae, J., Facchini, S., et al. 2021, ApJL, 916, L2, doi: [10.3847/2041-8213/ac0f83](https://doi.org/10.3847/2041-8213/ac0f83)
- Blakely, D., Francis, L., Johnstone, D., et al. 2022, ApJ, 931, 3, doi: [10.3847/1538-4357/ac6586](https://doi.org/10.3847/1538-4357/ac6586)
- Bradbury, J., Frostig, R., Hawkins, P., et al. 2018, JAX: composable transformations of Python+NumPy programs, 0.3.13. <http://github.com/google/jax>
- Broyden, C. G. 1970, IMA Journal of Applied Mathematics, 6, 76, doi: [10.1093/imamat/6.1.76](https://doi.org/10.1093/imamat/6.1.76)
- Buchner, J., Georgakakis, A., Nandra, K., et al. 2014, A&A, 564, A125, doi: [10.1051/0004-6361/201322971](https://doi.org/10.1051/0004-6361/201322971)
- Casassus, S., & Cárcamo, M. 2022, MNRAS, 513, 5790, doi: [10.1093/mnras/stac1285](https://doi.org/10.1093/mnras/stac1285)
- Christiaens, V., Cantalloube, F., Casassus, S., et al. 2019, ApJL, 877, L33, doi: [10.3847/2041-8213/ab212b](https://doi.org/10.3847/2041-8213/ab212b)
- Christiaens, V., Samland, M., Henning, T., et al. 2024, arXiv e-prints, arXiv:2403.04855, doi: [10.48550/arXiv.2403.04855](https://doi.org/10.48550/arXiv.2403.04855)
- Cugno, G., Patapis, P., Banzatti, A., et al. 2024, arXiv e-prints, arXiv:2404.07086, doi: [10.48550/arXiv.2404.07086](https://doi.org/10.48550/arXiv.2404.07086)
- Cugno, G., Patapis, P., Stolker, T., et al. 2021, A&A, 653, A12, doi: [10.1051/0004-6361/202140632](https://doi.org/10.1051/0004-6361/202140632)
- Currie, T., Lawson, K., Schneider, G., et al. 2022, Nature Astronomy, 6, 751, doi: [10.1038/s41550-022-01634-x](https://doi.org/10.1038/s41550-022-01634-x)
- Desdoigts, L., Pope, B. J. S., Dennis, J., & Tuthill, P. G. 2023, Journal of Astronomical Telescopes, Instruments, and Systems, 9, 028007. <https://api.semanticscholar.org/CorpusID:259297527>
- Dong, R., Hashimoto, J., Rafikov, R., et al. 2012, ApJ, 760, 111, doi: [10.1088/0004-637X/760/2/111](https://doi.org/10.1088/0004-637X/760/2/111)
- Doyon, R., Willott, C. J., Hutchings, J. B., et al. 2023, PASP, 135, 098001, doi: [10.1088/1538-3873/acd41b](https://doi.org/10.1088/1538-3873/acd41b)
- Facchini, S., Teague, R., Bae, J., et al. 2021, AJ, 162, 99, doi: [10.3847/1538-3881/abf0a4](https://doi.org/10.3847/1538-3881/abf0a4)
- Fletcher, R. 1970, The Computer Journal, 13, 317, doi: [10.1093/comjnl/13.3.317](https://doi.org/10.1093/comjnl/13.3.317)
- Foreman-Mackey, D. 2016, The Journal of Open Source Software, 1, 24, doi: [10.21105/joss.00024](https://doi.org/10.21105/joss.00024)
- Gaia Collaboration, Brown, A. G. A., Vallenari, A., et al. 2018, A&A, 616, A1, doi: [10.1051/0004-6361/201833051](https://doi.org/10.1051/0004-6361/201833051)

- Gaidos, E., Thanathibodee, T., Hoffman, A., et al. 2024, arXiv e-prints, arXiv:2403.09970, doi: [10.48550/arXiv.2403.09970](https://doi.org/10.48550/arXiv.2403.09970)
- Gallenne, A., Mérand, A., Kervella, P., et al. 2015, *A&A*, 579, A68, doi: [10.1051/0004-6361/201525917](https://doi.org/10.1051/0004-6361/201525917)
- Goldfarb, D. 1970, *Mathematics of Computation*, 24, 23. <http://www.jstor.org/stable/2004873>
- Goudfrooij, P., Grumm, D., Volk, K., & Bushouse, H. 2024, *PASP*, 136, 014503, doi: [10.1088/1538-3873/ad1c98](https://doi.org/10.1088/1538-3873/ad1c98)
- Haffert, S. Y., Bohn, A. J., de Boer, J., et al. 2019, *Nature Astronomy*, 3, 749, doi: [10.1038/s41550-019-0780-5](https://doi.org/10.1038/s41550-019-0780-5)
- Hammond, I., Christiaens, V., Price, D. J., et al. 2023, *MNRAS*, 522, L51, doi: [10.1093/mnras/slاد027](https://doi.org/10.1093/mnras/slاد027)
- Harris, C. R., Millman, K. J., van der Walt, S. J., et al. 2020, *Nature*, 585, 357, doi: [10.1038/s41586-020-2649-2](https://doi.org/10.1038/s41586-020-2649-2)
- Hashimoto, J., Dong, R., Kudo, T., et al. 2012, *ApJL*, 758, L19, doi: [10.1088/2041-8205/758/1/L19](https://doi.org/10.1088/2041-8205/758/1/L19)
- Helling, C., Dehn, M., Woitke, P., & Hauschildt, P. H. 2008, *ApJL*, 675, L105, doi: [10.1086/533462](https://doi.org/10.1086/533462)
- Helling, C., & Woitke, P. 2006, *A&A*, 455, 325, doi: [10.1051/0004-6361:20054598](https://doi.org/10.1051/0004-6361:20054598)
- Henyey, L. G., & Greenstein, J. L. 1941, *ApJ*, 93, 70, doi: [10.1086/144246](https://doi.org/10.1086/144246)
- Higson, E., Handley, W., Hobson, M., & Lasenby, A. 2018, *Statistics and Computing*, 29, 891–913, doi: [10.1007/s11222-018-9844-0](https://doi.org/10.1007/s11222-018-9844-0)
- Hunter, J. D. 2007, *Computing in Science & Engineering*, 9, 90, doi: [10.1109/MCSE.2007.55](https://doi.org/10.1109/MCSE.2007.55)
- Ireland, M. J. 2013, *MNRAS*, 433, 1718, doi: [10.1093/mnras/stt859](https://doi.org/10.1093/mnras/stt859)
- Isella, A., Benisty, M., Teague, R., et al. 2019, *ApJL*, 879, L25, doi: [10.3847/2041-8213/ab2a12](https://doi.org/10.3847/2041-8213/ab2a12)
- Juillard, S., Christiaens, V., & Absil, O. 2022, *A&A*, 668, A125, doi: [10.1051/0004-6361/202244402](https://doi.org/10.1051/0004-6361/202244402)
- Kammerer, J., Ireland, M. J., Martinache, F., & Girard, J. H. 2019, *MNRAS*, 486, 639, doi: [10.1093/mnras/stz882](https://doi.org/10.1093/mnras/stz882)
- Kammerer, J., Cooper, R. A., Vandal, T., et al. 2023, *PASP*, 135, 014502, doi: [10.1088/1538-3873/ac9a74](https://doi.org/10.1088/1538-3873/ac9a74)
- Keppler, M., Benisty, M., Müller, A., et al. 2018, *A&A*, 617, A44, doi: [10.1051/0004-6361/201832957](https://doi.org/10.1051/0004-6361/201832957)
- Keppler, M., Teague, R., Bae, J., et al. 2019, *A&A*, 625, A118, doi: [10.1051/0004-6361/201935034](https://doi.org/10.1051/0004-6361/201935034)
- Koposov, S., Speagle, J., Barbary, K., et al. 2023, [joshspeagle/dynesty: v2.1.0, v2.1.0](https://github.com/joshspeagle/dynesty), Zenodo, doi: [10.5281/zenodo.7600689](https://doi.org/10.5281/zenodo.7600689)
- Lucy, L. B. 1974, *AJ*, 79, 745, doi: [10.1086/111605](https://doi.org/10.1086/111605)
- Martinache, F. 2010, *ApJ*, 724, 464, doi: [10.1088/0004-637X/724/1/464](https://doi.org/10.1088/0004-637X/724/1/464)
- . 2013, *PASP*, 125, 422, doi: [10.1086/670670](https://doi.org/10.1086/670670)
- Martinache, F., Ceau, A., Laugier, R., et al. 2020, *A&A*, 636, A72, doi: [10.1051/0004-6361/201936981](https://doi.org/10.1051/0004-6361/201936981)
- Mesa, D., Keppler, M., Cantalloube, F., et al. 2019, *A&A*, 632, A25, doi: [10.1051/0004-6361/201936764](https://doi.org/10.1051/0004-6361/201936764)
- Müller, A., Keppler, M., Henning, T., et al. 2018, *A&A*, 617, L2, doi: [10.1051/0004-6361/201833584](https://doi.org/10.1051/0004-6361/201833584)
- Perotti, G., Christiaens, V., Henning, T., et al. 2023, *Nature*, 620, 516, doi: [10.1038/s41586-023-06317-9](https://doi.org/10.1038/s41586-023-06317-9)
- Plazas, A. A., Shapiro, C., Smith, R., Rhodes, J., & Huff, E. 2017, *Journal of Instrumentation*, 12, C04009, doi: [10.1088/1748-0221/12/04/C04009](https://doi.org/10.1088/1748-0221/12/04/C04009)
- Portilla-Revelo, B., Kamp, I., Rab, C., et al. 2022, *A&A*, 658, A89, doi: [10.1051/0004-6361/202141764](https://doi.org/10.1051/0004-6361/202141764)
- Portilla-Revelo, B., Kamp, I., Facchini, S., et al. 2023, *A&A*, 677, A76, doi: [10.1051/0004-6361/202346607](https://doi.org/10.1051/0004-6361/202346607)
- Ray, S., Sallum, S., Hinkley, S., et al. 2023, arXiv e-prints, arXiv:2310.11508, doi: [10.48550/arXiv.2310.11508](https://doi.org/10.48550/arXiv.2310.11508)
- Riaud, P., Mawet, D., Absil, O., et al. 2006, *A&A*, 458, 317, doi: [10.1051/0004-6361:20065232](https://doi.org/10.1051/0004-6361:20065232)
- Richardson, W. H. 1972, *Journal of the Optical Society of America* (1917-1983), 62, 55
- Ruffio, J.-B., Mawet, D., Czekala, I., et al. 2018, *AJ*, 156, 196, doi: [10.3847/1538-3881/aade95](https://doi.org/10.3847/1538-3881/aade95)
- Sallum, S., Eisner, J., Skemer, A., & Murray-Clay, R. 2023a, *ApJ*, 953, 55, doi: [10.3847/1538-4357/ace16c](https://doi.org/10.3847/1538-4357/ace16c)
- Sallum, S., Ray, S., Kammerer, J., et al. 2023b, arXiv e-prints, arXiv:2310.11499, doi: [10.48550/arXiv.2310.11499](https://doi.org/10.48550/arXiv.2310.11499)
- Shanno, D. F. 1970, *Mathematics of Computation*, 24, 647. <http://www.jstor.org/stable/2004840>
- Sissa, E., Gratton, R., Garufi, A., et al. 2018, *A&A*, 619, A160, doi: [10.1051/0004-6361/201732332](https://doi.org/10.1051/0004-6361/201732332)
- Sivaramakrishnan, A., Lafrenière, D., Ford, K. E. S., et al. 2012, in *Society of Photo-Optical Instrumentation Engineers (SPIE) Conference Series*, Vol. 8442, *Space Telescopes and Instrumentation 2012: Optical, Infrared, and Millimeter Wave*, ed. M. C. Clampin, G. G. Fazio, H. A. MacEwen, & J. Oschmann, Jacobus M., 84422S, doi: [10.1117/12.925565](https://doi.org/10.1117/12.925565)
- Sivaramakrishnan, A., Tuthill, P., Lloyd, J. P., et al. 2023, *PASP*, 135, 015003, doi: [10.1088/1538-3873/acaebd](https://doi.org/10.1088/1538-3873/acaebd)
- Skilling, J. 2004, in *American Institute of Physics Conference Series*, Vol. 735, *Bayesian Inference and Maximum Entropy Methods in Science and Engineering: 24th International Workshop on Bayesian Inference and Maximum Entropy Methods in Science and Engineering*, ed. R. Fischer, R. Preuss, & U. V. Toussaint, 395–405, doi: [10.1063/1.1835238](https://doi.org/10.1063/1.1835238)
- Skrutskie, M. F., Cutri, R. M., Stiening, R., et al. 2006, *The Astronomical Journal*, 131, 1163, doi: [10.1086/498708](https://doi.org/10.1086/498708)

- Soulain, A., & Robert C. M. T. 2023, AMICAL: Aperture Masking Interferometry Calibration and Analysis Library, Astrophysics Source Code Library, record ascl:2302.021
- Soulain, A., Sivaramakrishnan, A., Tuthill, P., et al. 2020, in Society of Photo-Optical Instrumentation Engineers (SPIE) Conference Series, Vol. 11446, Optical and Infrared Interferometry and Imaging VII, ed. P. G. Tuthill, A. Mérand, & S. Sallum, 1144611, doi: [10.1117/12.2560804](https://doi.org/10.1117/12.2560804)
- Speagle, J. S. 2020, MNRAS, 493, 3132, doi: [10.1093/mnras/staa278](https://doi.org/10.1093/mnras/staa278)
- Stolker, T., Dominik, C., Min, M., et al. 2016, A&A, 596, A70, doi: [10.1051/0004-6361/201629098](https://doi.org/10.1051/0004-6361/201629098)
- Stolker, T., Marleau, G. D., Cugno, G., et al. 2020a, A&A, 644, A13, doi: [10.1051/0004-6361/202038878](https://doi.org/10.1051/0004-6361/202038878)
- Stolker, T., Quanz, S. P., Todorov, K. O., et al. 2020b, A&A, 635, A182, doi: [10.1051/0004-6361/201937159](https://doi.org/10.1051/0004-6361/201937159)
- Stolker, T., Kammerer, J., Benisty, M., et al. 2024, A&A, 682, A101, doi: [10.1051/0004-6361/202347291](https://doi.org/10.1051/0004-6361/202347291)
- Thompson, W., Marois, C., Do Ó, C. R., et al. 2023a, AJ, 165, 29, doi: [10.3847/1538-3881/acalaf](https://doi.org/10.3847/1538-3881/acalaf)
- Thompson, W., Lawrence, J., Blakely, D., et al. 2023b, AJ, 166, 164, doi: [10.3847/1538-3881/acf5cc](https://doi.org/10.3847/1538-3881/acf5cc)
- Tierney, L., & Kadane, J. B. 1986, Journal of the American Statistical Association, 81, 82, doi: [10.1080/01621459.1986.10478240](https://doi.org/10.1080/01621459.1986.10478240)
- Wagner, K., Follete, K. B., Close, L. M., et al. 2018, ApJL, 863, L8, doi: [10.3847/2041-8213/aad695](https://doi.org/10.3847/2041-8213/aad695)
- Wagner, K., Stone, J., Skemer, A., et al. 2023, Nature Astronomy, 7, 1208, doi: [10.1038/s41550-023-02028-3](https://doi.org/10.1038/s41550-023-02028-3)
- Wang, J. J., Kulikaukas, M., & Blunt, S. 2021a, whereistheplanet: Predicting positions of directly imaged companions, Astrophysics Source Code Library, record ascl:2101.003
- Wang, J. J., Ginzburg, S., Ren, B., et al. 2020, AJ, 159, 263, doi: [10.3847/1538-3881/ab8aef](https://doi.org/10.3847/1538-3881/ab8aef)
- Wang, J. J., Vigan, A., Lacour, S., et al. 2021b, AJ, 161, 148, doi: [10.3847/1538-3881/abdb2d](https://doi.org/10.3847/1538-3881/abdb2d)
- Woitke, P., & Helling, C. 2003, A&A, 399, 297, doi: [10.1051/0004-6361:20021734](https://doi.org/10.1051/0004-6361:20021734)
- . 2004, A&A, 414, 335, doi: [10.1051/0004-6361:20031605](https://doi.org/10.1051/0004-6361:20031605)
- Wright, E. L., Eisenhardt, P. R. M., Mainzer, A. K., et al. 2010, The Astronomical Journal, 140, 1868, doi: [10.1088/0004-6256/140/6/1868](https://doi.org/10.1088/0004-6256/140/6/1868)

APPENDIX

A. MODEL FITTING RESULTS

A.1. *Disk Parameters*

Table 2 shows the derived disk parameters for the model that used uniform priors on the planet locations, as well as the model that used priors from Wang et al. (2021b). In both cases, we used Gaussian priors on the disk geometry, with the mean values taken from Keppler et al. (2018) and Keppler et al. (2019) and sensibly small standard deviation values chosen so as to break degeneracies between the disk model parameters, using the previously measured geometry of the disk. This was done because we are not primarily interested in independently measuring the parameters of the disk but wish to produce a sensible model of the disk emission so as to measure the emission from the known planets.

The derived disk parameters are nearly identical between the models using the two sets of planet location priors. This confirms what we see in the correlation plot in Figure 4, that there are no significant correlations between the disk parameters and the planet parameters that are biasing our results. If strong correlations were present we would see significant differences between the model disk parameters between the two cases.

A.2. *Planet Parameters*

In Table 3 we show the planet parameters, calculated using nested sampling, for both the model that used uniform priors on the locations of PDS 70 b and c, and the model that used the GRAVITY priors on the planet locations. The estimated systematic uncertainties in the contrast, separation and position angle, calculated in Section 3, are not included in the errors shown in Table 3.

A.3. *Image Plane Residuals*

In Figure 9 we plot the deconvolved image plane residuals from subtracting off different components of our PDS 70, disk, and planets model fit to the squared visibilities and closure phases. The deconvolved image plane residuals are primarily shown to verify the fitting to the interferometric observables and are not directly comparable to PSF subtracted direct images, due to the possibility of complex residual features introduced by the highly structured AMI PSF and the deconvolution process.

As also noted in the main text, we tentatively observe compact emission at a similar position to the mm emission seen by Balsalobre-Ruza et al. (2023) (top left panel of Figure 9.). The tentative compact emission seen in the image plane residuals is at the same position angle and is consistent with the signal that we see in the residual closure phases, shown in Figure 5. We note that the deconvolved image plane residuals are a poor diagnostic for measuring the noise in AMI data, because much of the residual signal is caused by differential piston errors (the dominant phase error term on the time scale of hours) to which the closure phase is immune. Thus, the SNR plots shown in Figure 5 give a much clearer picture of the level of signal left in the data after model removal of the disk and two planets, which gives us confidence in the detection of the compact emission to the south of PDS 70 A, as this cannot be caused by differential piston errors.

A.4. *SED Fit Parameters*

Table 4 shows the Drift-PHOENIX model parameters, with and without a blackbody component to model any excess CPD emission. We also report the Bayes factor, B_{12} , comparing each model with a blackbody component to the model without a blackbody component.

B. THE BRIGHTER-FATTER EFFECT

In Figure 10, we show the evolution of the pixel intensities for the central 9 pixels of the PSF, for PDS 70 and HD 123991. We show how the linearized ramp data evolves (blue), as each pixel accumulates signal, along with how this affects the calibrated rate data (red), output by the `jwst` pipeline (the `calints` data). We note that for the central pixel, the detected signal decreases, apparently at all signal levels, with the signal in most of the adjacent pixels either

Table 2. PDS 70 disk model parameters

Parameters	Prior	Uniform prior	GRAVITY prior
$\log A_a$ (arb.)	$\mathcal{U}(-10, -4)$	$-4.34^{+0.06}_{-0.09}$	$-4.34^{+0.07}_{-0.12}$
r_0 (as)	$\mathcal{U}(0.35, 0.65)$	$0.50^{+0.03}_{-0.03}$	$0.49^{+0.03}_{-0.03}$
FWHM_r (as)	$\mathcal{U}(0.03, 1.00)$	$0.22^{+0.04}_{-0.03}$	$0.22^{+0.06}_{-0.03}$
i ($^\circ$)	$\mathcal{N}(51.7, 1.0)^1$	$53.9^{+0.7}_{-0.8}$	$53.9^{+0.8}_{-0.8}$
P.A. ($^\circ$)	$\mathcal{N}(160.4, 1.0)^1$	$160.2^{+0.7}_{-0.7}$	$160.3^{+0.7}_{-0.6}$
$\log A_s$ (arb.)	$\mathcal{U}(-10, -4)$	$-8.4^{+1.1}_{-1.1}$	$-8.4^{+1.0}_{-1.0}$
H_{100} (au)	$\mathcal{N}(13, 5)^{2,3}$	$11.8^{+3.3}_{-3.3}$	$12.2^{+2.9}_{-3.2}$
β	$\mathcal{N}(1.25, 0.01)^2$	$1.25^{+0.01}_{-0.01}$	$1.25^{+0.01}_{-0.01}$
$\log I_o$ (arb.)	$\mathcal{U}(-10, -2)$	$-5.6^{+2.3}_{-2.8}$	$-6.2^{+2.6}_{-2.6}$
g	$\mathcal{U}(0, 1)$	$0.29^{+0.02}_{-0.01}$	$0.30^{+0.01}_{-0.01}$
α	$\mathcal{U}(0, 10)$	$0.7^{+0.9}_{-0.5}$	$0.8^{+1.6}_{-0.6}$

Notes: The median along with the 16th and 84th percentiles of the marginalized posteriors calculated with nested sampling are reported. $\mathcal{U}(a, b)$ denotes a uniform prior with lower and upper bounds a and b , respectively. $\mathcal{N}(\mu, \sigma)$ denotes a Gaussian prior, with mean μ and standard deviation σ .

¹ Reference: [Keppler et al. \(2019\)](#).

² Reference: [Keppler et al. \(2018\)](#), using the same distance as in the original paper of 113.43 pc ([Gaia Collaboration et al. 2018](#)).

³ Truncated to be positive.

Table 3. PDS 70 b and c parameters from nested sampling

	Sep. Prior (mas)	P.A. Prior ($^\circ$)	Separation (mas)	Position Angle ($^\circ$)	Contrast (Δmag)	Flux ($\text{W m}^{-2} \mu\text{m}^{-1}$)	SNR	$\log \mathcal{L}^{*2}$
PDS 70 b	$\mathcal{U}(100, 250)$	$\mathcal{U}(70, 160)$	$148.2^{+6.9}_{-7.8}$	$131.5^{+1.1}_{-1.1}$	$5.83^{+0.05}_{-0.05}$	$8.73^{+0.44}_{-0.40} \times 10^{-17}$	21.1	-30.0
	$\mathcal{N}(155.5, 1.4)^1$	$\mathcal{N}(132.7, 0.4)^1$	$155.0^{+1.4}_{-1.2}$	$132.3^{+0.4}_{-0.4}$	$5.82^{+0.04}_{-0.04}$	$8.85^{+0.35}_{-0.34} \times 10^{-17}$	27.9	-32.9
PDS 70 c	$\mathcal{U}(100, 250)$	$\mathcal{U}(230, 320)$	$221.3^{+4.8}_{-5.3}$	$269.7^{+1.2}_{-1.2}$	$6.47^{+0.10}_{-0.10}$	$4.82^{+0.46}_{-0.44} \times 10^{-17}$	10.6	–
	$\mathcal{N}(209.8, 1.0)^1$	$\mathcal{N}(270.1, 0.3)^1$	$210.4^{+0.9}_{-0.9}$	$270.1^{+0.3}_{-0.3}$	$6.61^{+0.09}_{-0.09}$	$4.24^{+0.38}_{-0.34} \times 10^{-17}$	11.9	–

Notes: The median along with the 16th and 84th percentiles of the marginalized posteriors are reported. $\mathcal{U}(a, b)$ denotes a uniform prior with lower and upper bounds a and b , respectively. $\mathcal{N}(\mu, \sigma)$ denotes a Gaussian prior, with mean μ and standard deviation σ .

¹ From the orbit posterior published in ([Wang et al. 2021b](#)), calculated using `whereistheplanet` ([Wang et al. 2021a](#)).

² $\log \mathcal{L}^*$ is the maximum likelihood of the full model including the star, both planets and the disk.

Table 4. Drift-PHOENIX SED model parameters for PDS 70 b and c

	T_{eff} (K)	$\log g$	[M/H]	R (R_J)	T_{disk} (K)	R_{disk} (R_J)	B_{12}
PDS 70 b	1339^{+26}_{-14}	$3.83^{+0.31}_{-0.78}$	$0.03^{+0.18}_{-0.23}$	$2.16^{+0.08}_{-0.14}$	–	–	–
	1404^{+26}_{-23}	$5.36^{+0.10}_{-0.18}$	$0.04^{+0.19}_{-0.20}$	$1.77^{+0.08}_{-0.07}$	207^{+19}_{-8}	1267^{+449}_{-568}	1.6×10^8
PDS 70 c	1031^{+26}_{-18}	$3.23^{+0.22}_{-0.16}$	$0.13^{+0.09}_{-0.15}$	$2.41^{+0.18}_{-0.17}$	–	–	–
	1050^{+43}_{-32}	$3.26^{+0.30}_{-0.18}$	$-0.00^{+0.18}_{-0.18}$	$2.19^{+0.18}_{-0.19}$	244^{+60}_{-22}	179^{+149}_{-128}	5.6

Notes: The median along with the 16th and 84th percentiles of the marginalized posteriors are reported. B_{12} is the Bayes factor between the blackbody CPD model and the no blackbody model.

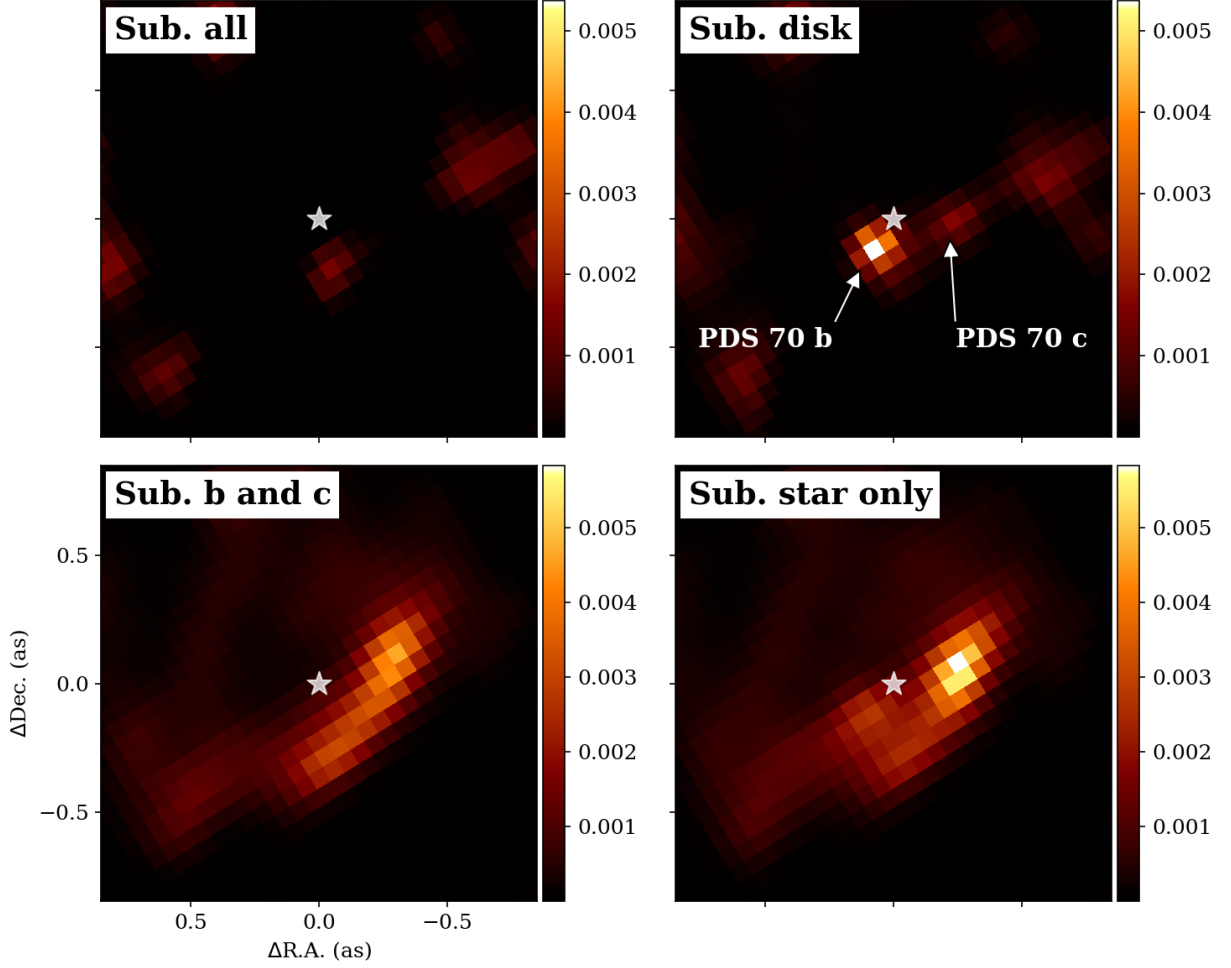


Figure 9. Deconvolved image plane residuals from subtracting the uniform planet prior model from the mean PDS 70 *calints* file. The data, and model image are smoothed by convolving it by a Gaussian kernel with $\sigma = 70$ mas to eliminate shifting artifacts and minimize photon noise. We then deconvolve the residuals with the smoothed calibrator PSF using 150 iterations of the Richardson-Lucy deconvolution algorithm (Richardson 1972; Lucy 1974). Each panel is shown in arbitrary linear units, with the top two panels and the bottom two panels each shown on the same scale. The top left shows the full residuals, the top right shows the residuals from subtracting off the star and disk, the bottom left shows the residuals from subtracting off the star and both planets and the bottom right shows the residuals from subtracting off the star.

rising or falling, with noticeable differences between PDS 70 and HD 123991. The chosen cutoff value, where we discard all data above this group, is denoted by the vertical dashed red line. For all pixels other than the central pixel, there is no significant signal deficit/excess up to this cutoff value.

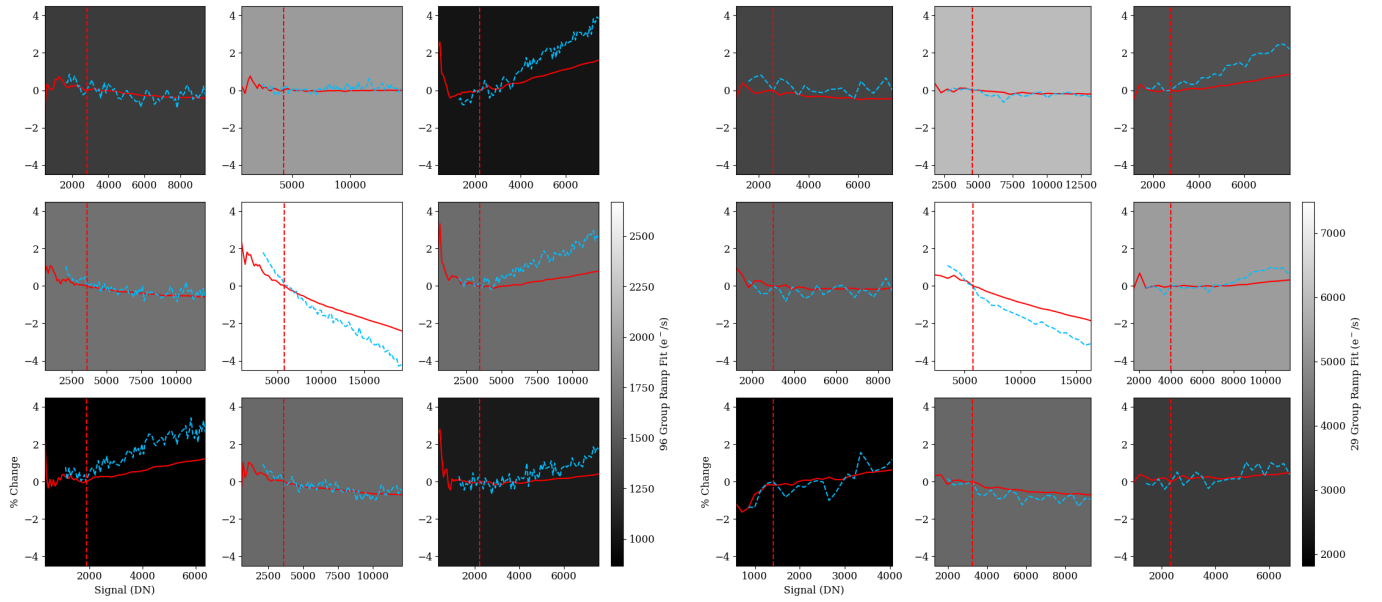


Figure 10. Evolution of the central 3×3 pixels as a function of the intensity in each pixel (in the linearized-ramp level data). PDS 70 is shown on the left and HD 123991 is shown on the right. The solid red line shows the evolution of the mean of the *calints* frames, after data cleaning. Here we are plotting the calculated rate minus the rate calculated from the first 28 groups and the first 10 groups, for PDS 70 and HD 123991, respectively. These rates are divided by the rate of the ramp fit using all of the groups. The dashed blue line shows the evolution of the linearized ramp-level data (ramp-level immediately after it has undergone the *linearity* step, in stage 1 of the *jwst* pipeline). To clearly illustrate the change in rate in each pixel as a function of well-depth, we are plotting the difference between groups separated by 15 groups and 5 groups for PDS 70 and HD 123991, respectively, for increasing signal. From this, we additionally subtract the difference between the 25th and 10th group for PDS 70 and the difference between the 10th group and the 5th group for HD 123991 and then normalize this quantity by the difference between the final group and one 15 and 5 groups earlier for PDS 70 and HD 123991, respectively. The vertical dashed red line shows the extent of the data that were used in our analysis.